Journal of Computational Electronics (2019) 18:628–639
https://doi.org/10.1007/s10825-019-01329-z

1 Tb/s all-optical XOR and AND gates using quantum-dot semiconductor optical amplifier-based turbo-switched Mach–Zehnder interferometer

Amer Kotb[1,2] · **Kyriakos E. Zoiros**[3] · **Chunlei Guo**[1,4]

Abstract

The turbo-switch (TS) architecture conceived for speeding up the response of conventional semiconductor optical amplifiers (SOAs) is combined for the first time with the exceptional ultrafast capability of quantum-dot (QD) SOAs. The possibility of exploiting this combination in the Mach–Zehnder interferometer (MZI) for implementing fundamental all-optical (AO) XOR and AND logic gates run at 1 Tb/s is numerically investigated, assessed, and verified. The simulation results demonstrate the superiority of the QDSOA-based TS-MZI scheme over its QDSOA-based MZI counterpart, as quantified by the improved quality factor, which can be achieved under more favorable operating conditions. The outcomes of the conducted theoretical treatment can help execute AO signal processing tasks with enhanced performance while keeping pace with the perpetual increase of single-channel data rates in an efficient and affordable manner.

Keywords All-optical XOR gate · All-optical AND gate · Quantum-dot semiconductor optical amplifier · Turbo-switch · Mach–Zehnder interferometer

1 Introduction

In recent years, the increase of single-channel data rates above 100 Gb/s [1] and the upgrade of aggregate capacities well into the Tb/s region [2] to cope with the huge amount of information in modern communication networks has made indispensable executing signal processing tasks entirely in the optical domain, i.e., all-optically (AO) [3], instead of resorting to cumbersome optical-to-electrical-to-optical conversions that cannot bridge the gap in bandwidth handling capability between fibers and electronics. To serve this purpose, semiconductor optical amplifiers (SOAs) have widely been employed as the technological platform [4–6] owing to their strong nonlinearities, reasonable power consumption, broad gain bandwidth, small footprint, and amenability to scalable integration in single chips at an affordable cost [7]. Despite these attractive properties, the exploitation of SOAs in AO applications is compromised by the finite SOA carrier recovery time, which results in pattern-dependent dynamic behavior and consequently performance degradation as bit rates get higher [8]. Two notable paths that have been followed so far to confront this problem include (a) devising sophisticated architectures, such as the turbo-switch (TS), where a pair of SOAs is cascaded and separated by broadband optical filters (OFs) [9, 10]. The extra SOA acts as a nonlinear filter to compensate for the slow recovery component of the signal emerging from the first SOA, thus shortening the overall gain and phase response time of the whole SOAs combination over the single SOA. In this manner, the deleterious pattern effects can be strongly suppressed to support operation at higher data rates while avoiding the degradation of the optical signal-to-noise ratio

---

✉ Amer Kotb
amer@ciomp.ac.cn

✉ Chunlei Guo
guo@optics.rochester.edu

[1] The Guo China-US Photonics Laboratory, Changchun Institute of Optics, Fine Mechanics, and Physics, Chinese Academy of Sciences, Changchun 130033, China

[2] Department of Physics, Faculty of Science, University of Fayoum, Fayoum 63514, Egypt

[3] Lightwave Communications Research Group, Department of Electrical and Computer Engineering, School of Engineering, Democritus University of Thrace, 67100 Xanthi, Greece

[4] The Institute of Optics, University of Rochester, Rochester, NY 14627, USA

that would otherwise occur if linear narrow band OFs were used instead [11]. The TS principle of operation and speed enhancement action has been theoretically analyzed [12, 13] and experimentally characterized [14], while this configuration has been practically implemented and applied to allow for faster AO switching functionalities [15, 16]. In this context, it has also been suggested that the TS should better be placed in both arms of the Mach–Zehnder interferometer (MZI) [17–19], since doing so holds the promise of allowing accomplishing switching at speeds that can keep pace with the ongoing trend in single-channel data rates. The MZI effectively combines the structural simplicity, the co-propagation of the launched signals, the possibility to independently control the phase in each arm, the compact size, the thermal stability, the reasonable switching energy requirement, the regeneration capability, the integrability, and overall practicality [20]. The modified architecture is known as the turbo-switched Mach–Zehnder interferometer (TS-MZI). (b) Developing internal nanometric structures referred to as quantum-dot semiconductor optical amplifiers (QDSOAs) [21] in order to directly reduce the carrier relaxation time, which is not done with approach (a). Compared to conventional SOAs, QDSOAs exhibit lower current density threshold, higher saturation output power, wider gain bandwidth, lower noise figure, similarly low polarization gain dependence, weaker thermal dependence [22–24], and above all, faster gain recovery time [25]. These features have rendered QDSOAs ideal candidates for AO signal processing applications where ultrafast operation with pattern-free performance is pursued [26–34]. According to (a) and (b), it is natural to ask what would happen if the individual ultrafast potential of the TS-MZI were combined with that of QDSOAs by incorporating the latter into the former in a common all-optical switching platform. Thus, in this paper, we theoretically explore this possibility and provide a positive answer to the above rational question with respect to the realization of the fundamental XOR and AND logic gates. The results obtained through numerical simulations demonstrate indeed the feasibility of using the QDSOA-based TS-MZI scheme to execute the target Boolean functions at 1 Tb/s with better performance than the standard QDSOA-based MZI.

2 Principle of operation

2.1 Basic QDSOA-based TS-MZI

Figure 1a shows the schematic diagram of the QDSOA-based TS-MZI, which is employed as the core logic module for implementing the target XOR and AND Boolean functions. The structure is conceived from the typical SOA-based MZI geometry depicted in Fig. 1b but with bulk SOAs in the MZI branches replaced by QDSOAs and every single active element replaced by two identical devices, which are separated by broadband OFs. In the simplest form of this modified configuration, sufficiently strong switching signals (also referred to as ‘pump’), which may originate from the same or different optical sources, perturb the dynamics of QDSOA1 and QDSOA2 and cross-modulate the phase of the split components that travel along the corresponding MZI paths of a weaker signal to be switched (also termed as ‘probe’). After perceiving the switching signal effects inside the leftmost top and bottom QDSOAs, the probe components encounter two optical filters in their path, OF1 and OF2, which allow only them to pass through while blocking the corresponding pump signals. The filtered components enter QDSOAs 3 and 4, where due to self-gain modulation mechanism [35] the gain of QDSOAs 3 and 4 is increased, while the modulated probe amplitude is low and is decreased as the modulated probe amplitude recovers. Because the gain recovery of these additional QDSOAs is finite, their self-gain dynamics compensate for the slower part of the probe signals amplitude coming out of QDSOAs 1 and 2, thereby accelerating amplitude restoration and resulting in considerably less pattern-dependent affected switching performance [14]. This is shown in Fig. 2, which depicts the dynamics of the individual gain contributions after QDSOA1 and QDSOA3 for the AO AND logic operation. From this figure, it can be seen that although the QDSOA1 gain response suffers from pattern effects, which manifest as peak-to-peak amplitude fluctuation, these are compensated by the following QDSOA3. In this manner, and depending on the dynamic control exerted by the switching signals, the phase difference incurred on the copies of the signal to be

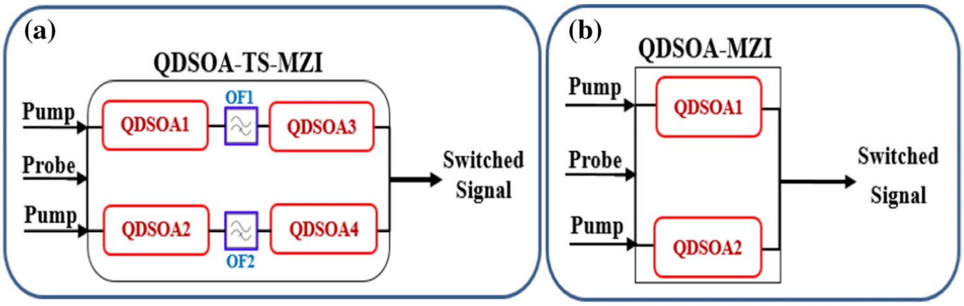

Fig. 1 Schematic diagram of **a** QDSOA-based TS-MZI, **b** QDSOA-based MZI. OF: broadband optical filter

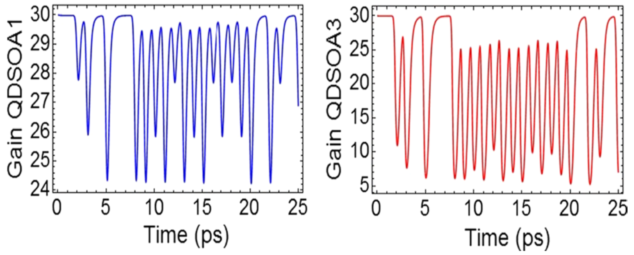

Fig. 2 Dynamics of gain contributions after QDSOA1 and QDSOA3 for AND operation

switched is converted by the MZI into amplitude change at the output, aiming at achieving the binary outcome of the target logic operations.

2.2 XOR gate with QDSOA-based TS-MZI

The schematic diagram and truth table of the AO XOR gate using the QDSOA-based TS-MZI is shown in Fig. 3.

A continuous wave (CW) signal at λ_{XOR}, which is the assigned output signal wavelength, is injected from port 2 into the QDSOA-TS-MZI middle arm and is equally split by a 3-dB optical coupler (OC). Using wavelength selective couplers (WSCs), the CW half traveling in the upper MZI arm is combined with data signal A at wavelength λ_A inserted from port 1, while the other CW half propagating along the lower MZI arm is combined with data signal B at wavelength λ_B (which can be the same as λ_A) inserted from port 3. Data signals A and B perturb QDSOA1 and QDSOA2 dynamics and alter the phase of the CW beam on which the outcome of switching is mapped and transferred at the MZI output. When both A and B are logically the same, i.e., '0' or '1,' the structure remains dynamically balanced, and thus, no differential phase shift is imparted between the CW constituents, which therefore cancel each other when they recombine at OC located at port 4 and so the MZI output remains at low amplitude level, i.e., '0.' In contrast, when the binary content of A and B differs, the MZI dynamic symmetry is broken and the CW copy that is cross-modulated by either A or B acquires a phase shift relative to its counterpart, which is translated into amplitude modulation of high level, i.e., '1,' at the MZI output. In this manner, the XOR operation is executed according to its truth table.

2.3 AND gate with QDSOA-based TS-MZI

The schematic diagram and truth table of the AO AND gate using the QDSOA-based TS-MZI is shown in Fig. 4.

For AND operation, data A and its delayed replica centered at λ_A are injected into the QDSOA-TS-MZI upper and lower arms, respectively. Concurrently, data B centered at the target output signal wavelength λ_{AND} is inserted into the middle arm of the interferometric scheme and is equally divided using a 3 dB OC before being combined via WSCs with data A and its delayed copy inside QDSOA1 and QDSOA2, respectively. Because data A and its lagging version modify the optical properties of these QDSOAs at different instants,

Fig. 3 Schematic diagram and truth table of AO XOR gate using QDSOA-based TS-MZI. OC: 3 dB optical coupler. WSC: wavelength selective coupler. OF: broadband optical filter

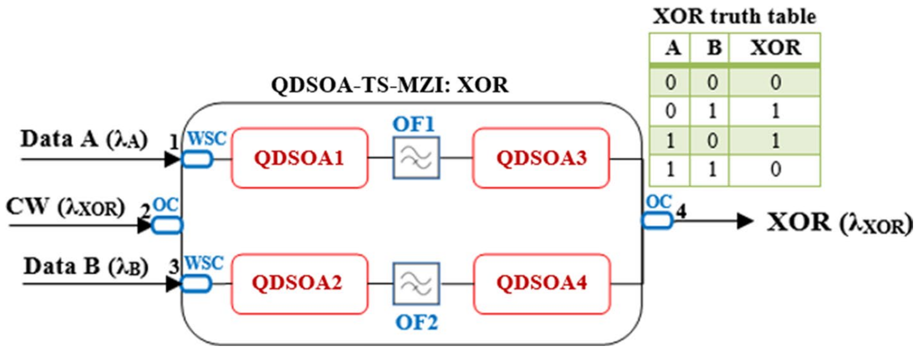

XOR truth table

A	B	XOR
0	0	0
0	1	1
1	0	1
1	1	0

Fig. 4 Schematic diagram and truth table of AO AND gate using QDSOA-based TS-MZI. OC: 3 dB optical coupler. WSC: wavelength selective coupler. OF: broadband optical filter

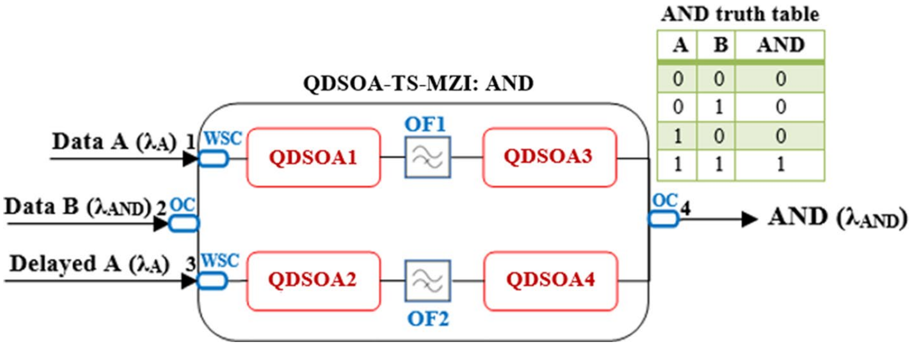

AND truth table

A	B	AND
0	0	0
0	1	0
1	0	0
1	1	1

the phase shifts on the corresponding split components of data B that manifest through cross-modulation are induced with a relative delay. This creates a phase switching window, which is open when both data signals A and B are enabled, i.e., contain a logic ‘1,’ whereas it is closed for any other logic combination of these inputs. In this manner, a pulse is produced only in the former case, as opposed to the latter for which no pulse is delivered, and so according to the respective truth table, the operation subject to these conditions forms an AO AND gate. It should be pointed out that although the switching speed is not determined by the recovery time of the active elements but by the inverse of the delay deliberately introduced on one input of data A [36], this fact is not sufficient on its own to achieve ultrafast rates of the order of Tb/s. This underlines the need to devise, design, apply, and combine advanced structures and ingenious techniques, as pursued in this contribution through a combination of the QDSOAs and the TS switch on the MZI platform.

3 Modeling

3.1 QDSOA

In this paper, QDSOAs are modeled using a two-level model in the QD conduction band [31, 37]. The carriers produced in the wetting layer (WL) via the injection current pass through an intermediate state, which acts as the carrier reservoir, and make the transition to the GS, whose density determines the output gain. These transitions result in photon emission from the conduction band to the valence band. This process is schematically shown in Fig. 5.

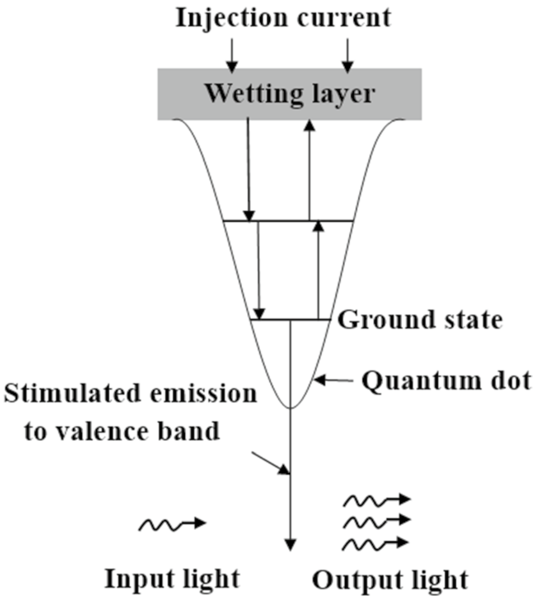

Fig. 5 Schematic diagram of QDs states and carriers transitions

The nonlinear effect of ‘Carrier Heating’ (CH) results from carriers’ thermalization in the entire energy band following the pulse. This process occurs on a very short time scale between 0.1 and 0.7 ps. The pulse energy reduces the optical gain at the photon energy of this excitation and burns a hole in the gain spectrum, which is a nonlinear effect known as ‘Spectral Hole Burning’ (SHB). By taking into account both CH and SHB, the time-dependent gain of each QDSOA is described by the following coupled first-order differential equations [31, 37]:

$$\frac{\mathrm{d}h_d(t)}{\mathrm{d}t} = \frac{h_w(t)}{\tau_{dw}}\left(1 - \frac{h_d(t)}{h_0}\right) - \frac{h_d(t)}{\tau_{dr}} - \left(\exp\left[h_d(t) + h_{\mathrm{CH}}(t) + h_{\mathrm{SHB}}(t)\right] - 1\right)\frac{P_{\mathrm{in,\,QDSOA}_i}(t)}{E_{\mathrm{sat}}} \tag{1}$$

$$\frac{\mathrm{d}h_w(t)}{\mathrm{d}t} = \frac{h_{\mathrm{in}}}{\tau_{wr}}\left(1 - \frac{h_w(t)}{h_0}\right) - \frac{h_w(t)}{\tau_{wr}} - \frac{h_w(t)}{\tau_{wd}}\left(1 - \frac{h_d(t)}{h_0}\right) \tag{2}$$

$$\frac{\mathrm{d}h_{\mathrm{CH}}(t)}{\mathrm{d}t} = -\frac{h_{\mathrm{CH}}(t)}{\tau_{\mathrm{CH}}} - \frac{\varepsilon_{\mathrm{CH}}}{\tau_{\mathrm{CH}}}\left(\exp\left[h_d(t) + h_{\mathrm{CH}}(t) + h_{\mathrm{SHB}}(t)\right] - 1\right) P_{\mathrm{in,\,QDSOA}_i}(t) \tag{3}$$

$$\frac{\mathrm{d}h_{\mathrm{SHB}}(t)}{\mathrm{d}t} = -\frac{h_{\mathrm{SHB}}(t)}{\tau_{\mathrm{SHB}}} - \frac{\varepsilon_{\mathrm{SHB}}}{\tau_{\mathrm{SHB}}}\left(\exp\left[h_d(t) + h_{\mathrm{SHB}}(t) + h_{\mathrm{CH}}(t)\right] - 1\right) P_{\mathrm{in,\,QDSOA}_i}(t) - \frac{\mathrm{d}h_d(t)}{\mathrm{d}t} - \frac{\mathrm{d}h_{\mathrm{CH}}(t)}{\mathrm{d}t} \tag{4}$$

$$h_{\mathrm{in}} = \int_0^z \frac{a J \tau_{wr}}{ed}\,\mathrm{d}z' \tag{5}$$

where functions ‘h’ represent the QDSOA power gain integrated over its longitudinal dimension, $z \in [0, L]$, where L is the QDSOA length, for carriers recombination between QDs states (h_d) and WL (h_w), carrier heating (h_{CH}), and spectral hole burning (h_{SHB}). $h_0 = \ln[G_0]$, where G_0 is the unsaturated power gain, E_{sat} is the saturation energy, and $P_{\mathrm{in,\,QDSOA}_i}(t)$ is the input power to each QDSOA involved in the QDSOA-TS-MZI (denoted by index $i = 1, 2, 3, 4$). τ_{dw} is the excitation rate from QD GS to WL, and τ_{dr} is the recombination rate of QD. τ_{wd} is the transition rate from WL to QD GS, and τ_{wr} is the carrier recombination rate of WL. τ_{CH} and τ_{SHB} are the temperature relaxation rate and the carrier–carrier scattering rate, respectively. $\varepsilon_{\mathrm{CH}}$ and $\varepsilon_{\mathrm{SHB}}$ are the nonlinear gain suppression factors due to CH and SHB, respectively. α is the differential gain, which represents the ratio of carriers in WL and QDs, J is the injection current density, d is the thickness of the WL, and e is the electron charge. The total gain of each QDSOA is given by [38]:

$$G_{\mathrm{QDSOA}_i}(t) = \exp\left[h_d(t) + h_{\mathrm{CH}}(t) + h_{\mathrm{SHB}}(t)\right], \quad i = 1,\ 2,\ 3,\ 4 \tag{6}$$

while the phase change incurred on the signal propagating in each QSOA is given by [36]:

$$\Phi_{\mathrm{QDSOA}_i}(t) = -0.5\left(\alpha\, h_d(t) + \alpha_{\mathrm{CH}}\, h_{\mathrm{CH}}(t) + \alpha_{\mathrm{SHB}}\, h_{\mathrm{SHB}}(t)\right), \quad i = 1,\ 2,\ 3,\ 4 \tag{7}$$

where α is the traditional linewidth enhancement factor (α-factor), which strongly affects the efficiency of cross-phase modulation exploited for all-optical switching, and α_{CH} and α_{SHB} are the linewidth enhancement factors due to CH and SHB, respectively. α_{SHB} is zero because SHB produces a nearly symmetrical spectral hole centered at the signal wavelength [39].

3.2 OF

The OF is assumed to be a Gaussian-shaped optical bandpass filter whose field transfer function is conveniently expressed in the frequency domain [40]:

$$\mathrm{OF}_{1,2}(f) = \exp\left[-\ln\left[\sqrt{2}\right]\left(\frac{f-f_{\mathrm{c}}}{B/2}\right)^{2N}\right] \tag{8}$$

where f is the frequency of the input signal and f_{c} is the center frequency of the filter. B is the filter bandwidth, which is chosen to exceed the value determined by the target operation bit rate, i.e., ≥ 1 THz, so that the memory effect of the filter in the time domain is negligible [41]. N is the filter's order which determines the sharpness of its passband edges [42], where $N = 1$ corresponds to Gaussian and $N \geq 2$ to super-Gaussian shapes.

3.3 Input and output signals

3.3.1 Data

The data signals are assumed to exhibit a Gaussian power profile in the time domain:

$$P_{A,B}(t) = \sum_{n=1}^{p} \left\{a_n\right\}_{A,B} P_{\mathrm{peak}} \exp\left[-\frac{4\ln 2(t - nT)^2}{\tau_{\mathrm{FWHM}}^2}\right] \tag{9}$$

where the code $\left\{a_n\right\}_{A,B}$ takes the binary value '1' or '0' with equal probability inside a pseudorandom binary sequence (PRBS) of length $p = 2^7 - 1$ that contains pulses having period $T = 1$ ps, peak power (P_{peak}), and full-width at half-maximum (FWHM) pulse width (τ_{FWHM}) such that the duty cycle is 30%.

3.3.2 XOR

For XOR operation, the power of the signals inserted into QDSOA1 and QDSOA2 is given by:

$$P_{\mathrm{in,\,QDSOA}_1}(t) = P_A(t) + 0.5\,P_{\mathrm{CW}} \tag{10}$$

$$P_{\mathrm{in,\,QDSOA}_2}(t) = 0.5\,P_{\mathrm{CW}} + P_B(t) \tag{11}$$

where the coefficient '0.5' takes into account the coupling of the CW beam of power P_{CW} into the MZI arms. The power inserted into QDSOA3 and QDSOA4 is that of the signals coming out of OF1 and OF2, respectively, which is analogous to the square modulus of the corresponding complex electric field, $E_{\mathrm{OF}_{1,2}}(t)$ [42]:

$$\begin{aligned} P_{\mathrm{in,\,QDSOA}_{3,4}} \equiv P_{\mathrm{OF}_{1,2}}(t) &= \left|E_{\mathrm{OF}_{1,2}}(t)\right|^2 \\ &= \left|F^{-1}\left[F\left[E_{\mathrm{out,\,QDSOA}_{1,2}}(t)\right] \cdot \mathrm{OF}_{1,2}\left[f\right]\right]\right|^2 \end{aligned} \tag{12}$$

where operators $F[\cdot]$ and $F^{-1}[\cdot]$denote the Fourier transform and its inverse, respectively. $E_{\mathrm{out,\,QDSOA}_{1,2}}(t)$ is the complex electric field of the signal emerging from QDSOA1 and QDSOA2, respectively. This is found by applying the amplitude gain and phase calculated from (6) and (7), respectively, after solving (1)–(5) for QDSOAs input power given from (10) and (11), to the complex electric field of the halved CW signal going into QDSOA1 and QDSOA2 [38]:

$$\begin{aligned} E_{\mathrm{out,\,QDSOA}_{1,2}}(t) = \sqrt{0.5P_{\mathrm{CW}}}\, \exp\Big[0.5\, \ln\left[G_{\mathrm{QDSOA}_{1,2}}(t)\right] \\ + j\Phi_{\mathrm{QDSOA}_{1,2}}(t)\Big] \end{aligned} \tag{13}$$

3.3.3 AND

For AND operation, the power of the signals inserted into QDSOA1 and QDSOA2 is given by:

$$P_{\mathrm{in,\,QDSOA}_1}(t) = P_{\mathrm{A}}(t) + 0.5\,P_{\mathrm{B}}(t) \tag{14}$$

$$P_{\mathrm{in,\,QDSOA}_2}(t) = 0.5\,P_{\mathrm{B}}(t) + P_{\mathrm{A}}(t - \Delta\tau) \tag{15}$$

where the coefficient '0.5' takes into account the coupling of data signal B of power P_{B} into the MZI arms and $\Delta\tau$ is the time delay of the temporally lagging copy of data signal A.

The complex electric field of the signal coming out of QDSOA1 and QDSOA2 and inserted into QDSOA3 and QDSOA4, respectively, is given by:

$$\begin{aligned} E_{\mathrm{out,\,QDSOA}_{1,2}}(t) = \sqrt{0.5P_{\mathrm{B}}(t)}\, \exp\Big[0.5\, \ln\left[G_{\mathrm{QDSOA}_{1,2}}(t)\right] \\ + j\,\Phi_{\mathrm{QDSOA}_{1,2}}(t)\Big] \end{aligned} \tag{16}$$

3.4 MZI

For both gates implemented with the QDSOA-TS-MZI scheme, their time-dependent output power is calculated by combining the electric field of the signal emerging from QDSOA3 and QDSOA4 into the OC at MZI port 4. Using the mathematical formulation for the operation of this passive element gives [43]:

$$P_{\text{out, XOR/AND}}(t) = 0.5\left(\left|E_{\text{out, QDSOA}_3}(t)\right|^2 + \left|E_{\text{out, QDSOA}_4}(t)\right|^2\right) + \left|E_{\text{out, QDSOA}_3}(t)\right|\left|E_{\text{out, QDSOA}_4}(t)\right| \sin\left[\Phi_{\text{QDSOA}_3}(t) - \Phi_{\text{QDSOA}_4}(t)\right] \tag{17}$$

with

$$E_{\text{out, QDSOA}_{3,4}}(t) = E_{\text{OF}_{1,2}}(t)\exp\left[0.5\ln\left[G_{\text{QDSOA}_{3,4}}(t)\right] + j\,\Phi_{\text{QDSOA}_{3,4}}(t)\right] \tag{18}$$

where $E_{\text{OF}_{1,2}}(t)$, $P_{\text{in, QDSOA}_{3,4}}(t)$ and $G_{\text{QDSOA}_{3,4}}(t)$, $\Phi_{\text{QDSOA}_{3,4}}(t)$ are known through (12) and (6)–(7), respectively. In Eq. (17), the sinusoidal term, whose argument includes the relative difference of the phase shifts induced inside $\text{QDSOA}_{3,4}$, reflects the fact that the outputs of $\text{QDSOA}_{3,4}$, which exhibit the same wavelength, are added coherently at the MZI exit.

On the other hand, when both gates are implemented with the conventional QDSOA-MZI scheme, i.e., using only QDSOA1 and QDSOA2, their output power is described by the standard interferometric equation [20]:

$$P_{\text{out, XOR/AND}}(t) = 0.25\,P_{\text{CW/B}}\left(G_{\text{QDSOA}_1}(t) + G_{\text{QDSOA}_2}(t) - 2\sqrt{G_{\text{QDSOA}_1}(t)\,G_{\text{QDSOA}_2}(t)}\cos\left[\Phi_{\text{QDSOA}_1}(t) - \Phi_{\text{QDSOA}_2}(t)\right]\right) \tag{19}$$

4 Results

In this theoretical treatment, the performance of the AO XOR and AND gates has been investigated by examining and evaluating the dependence of the quality factor (QF) on the input signals and QDSOAs critical parameters. For this purpose, the rate equations (1)–(4) have been numerically solved using Adams' numerical method and implementing it in Mathematica® for the default parameters' values cited in Table 1. These values are consistent with literature [28–33] that has used QDSOAs of similar geometrical and physical properties as those considered in this work. The QF is defined as $\text{QF} = (P_1 - P_0)/(\sigma_1 + \sigma_0)$ [37], where P_1, P_0 denote the average power of the logically outcoming '1' and '0' data, while σ_1, σ_0 denote the corresponding standard deviations. In order to ensure that the related bit-error rate is smaller than 10^{-9}, the QF should be kept over six in order [31–33]. Besides pattern effects, in this simulation we also account for the possible deviation of the shape of the logically outcoming pulses against the input ones [19]. For this purpose, we have used the cross-correlation (XC) coefficient [44], which provides a measure of the degree of similarity between the intensity profile of the switched pulses and the corresponding profile prior to the same pulses being inserted in the MZI (with XC = 100% implying perfect match).

4.1 XOR

Figures 6 and 7 show the simulation results for the logic pulse profiles and corresponding pseudo-eye diagrams (PED) [17] for the AO XOR operation using the QDSOA-TS-MZI and the QDSOA-MZI at 1 Tb/s. The obtained values of the QF are 18.5 and 7.9, respectively. The obtained QFs are 18.5 and 7.9, respectively. It should be noted that the very high QF in the former case is due to the statistical approach followed, by definition of the QF, to calculate the QF within the frame of this as well as other similar numerical analyses. For this reason, it is common practice to obtain values of this metric which are far in excess of its lower permissible limit. Although such high values are not realistic in terms of the related BER [45], they are very useful for the sake of theoretically comparing the performance of different AO schemes, as done in this paper via Figs. 6, 7, 8, 9, 10, 11, 12, 13, and 14. Therefore, QF values as high as 18.5, which are attained in the paper, do make sense for the purposes of this study and thus are analogously interpreted. The numerical difference of the above QFs reflects the fact that the spaces obtained when both data signals are 'on,' which is the ultimate challenge for the performance of an XOR gate [46], are fully extinguished by the QDSOA-TS-MZI, while they exhibit small but discernible peaks with the QDSOA-MZI. This is also seen in the PEDs, where the border of the low binary level is uniformly thick in the former case, but it degenerates from the perfect '0' ground in the latter. On the

Table 1 Simulation parameters default values

Symbol	Definition	Value	Unit
E_0	Pulse energy	20	fJ
τ_{FWHM}	Pulse width	0.3	ps
T	Bit period	1	ps
p	PRBS length	127	–
f_{A}	Frequency of data A (XOR operation)	189.7	THz
f_{B}	Frequency of data B (XOR operation)	189.7	THz
f_{CW}	Frequency of CW (XOR operation)	194.7	THz
f_{c}	Center frequency of filter (XOR operation)	194.7	THz
P_{A}	Power of data A (XOR operation)	1	mW
P_{B}	Power of data B (XOR operation)	1	mW
P_{CW}	Power of CW (XOR operation)	2	mW
f_{A}	Frequency of data A (AND operation)	189.82	THz
$f_{\mathrm{delayed\ A}}$	Frequency of delayed A (AND operation)	189.82	THz
f_{B}	Frequency of data B (AND operation)	194.83	THz
f_{c}	Center frequency of filter (AND operation)	194.83	THz
P_{A}	Power of data A (AND operation)	0.4	mW
$P_{\mathrm{delayed\ A}}$	Power of delayed A (AND operation)	0.4	mW
P_{B}	Power of data B (AND operation)	0.001	mW
B	Optical bandwidth of filter	1.8	THz
N	Order of filter	2	–
$\Delta\tau$	Time delay (AND operation)	0.15	ps
J	Injection current density	5	kA/cm^2
N_{ES}	Carriers density in QD ES	7.2×10^{-18}	cm^3
N_{GS}	Carriers density in QD GS	3.6×10^{-18}	cm^3
E_{sat}	Saturation energy	0.045	pJ
τ_{wd}	Transition rate from WL to QDs state	5	ps
τ_{dw}	Excitation rate from QDs state to WL	10	ns
τ_{wr}	Carrier recombination rate in WL	2.2	ns
τ_{dr}	Carrier recombination rate in QDs state	0.4	ns
τ_{CH}	Temperature relaxation rate	0.3	ps
τ_{SHB}	Carrier-carrier scattering rate	0.1	ps
α	Traditional α-factor	4	–
α_{CH}	CH α-factor	1	–
α_{SHB}	SHB α-factor	0	–
$\varepsilon_{\mathrm{CH}}$	CH nonlinear gain suppression factor	0.02	W^{-1}
$\varepsilon_{\mathrm{SHB}}$	SHB nonlinear gain suppression factor	0.02	W^{-1}
Γ	Confinement factor	0.15	–
α	Differential gain	8.6×10^{-15}	cm^{-2}
d	WL thickness	0.5	μm
L	Length of QDSOA active region	1	mm
G_0	Unsaturated power gain	30	dB

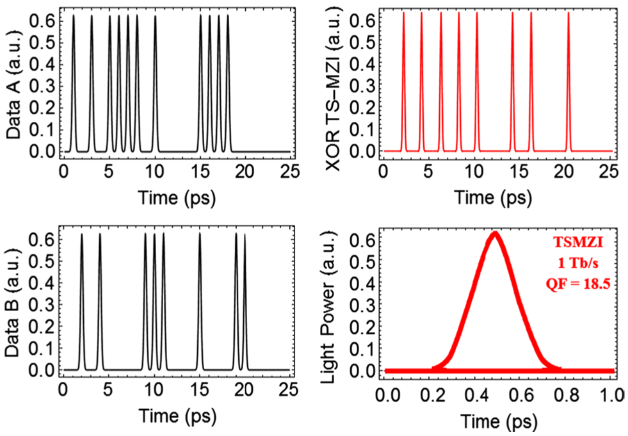

Fig. 6 Simulation results for XOR operation with QDSOA-based TS-MZI at 1 Tb/s

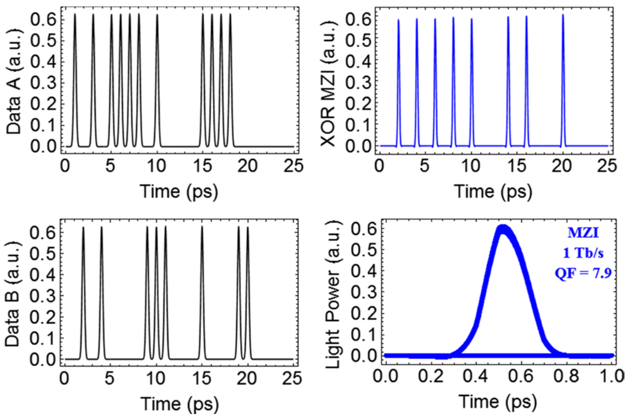

Fig. 7 Simulation results for XOR operation with QDSOA-based MZI at 1 Tb/s

other hand, the calculated XC is 95% when using the TS-MZI, which indicates that the switched data pulse envelope deviates by only 5% from that inserted in the configuration. The numerically obtained XC value is 89% when using the conventional MZI.

Figures 8 and 9 depict the QF dependence on several parameters which are critical for the operation of the AO logic system. More specifically, these include the data A, B input peak power (Fig. 8a), QDSOAs traditional linewidth enhancement factor (α-factor) (Fig. 8b), QDSOAs injection current density (Fig. 9a), and QDSOAs transition rate from WL to QDs ground state (Fig. 9b). For comparison, results

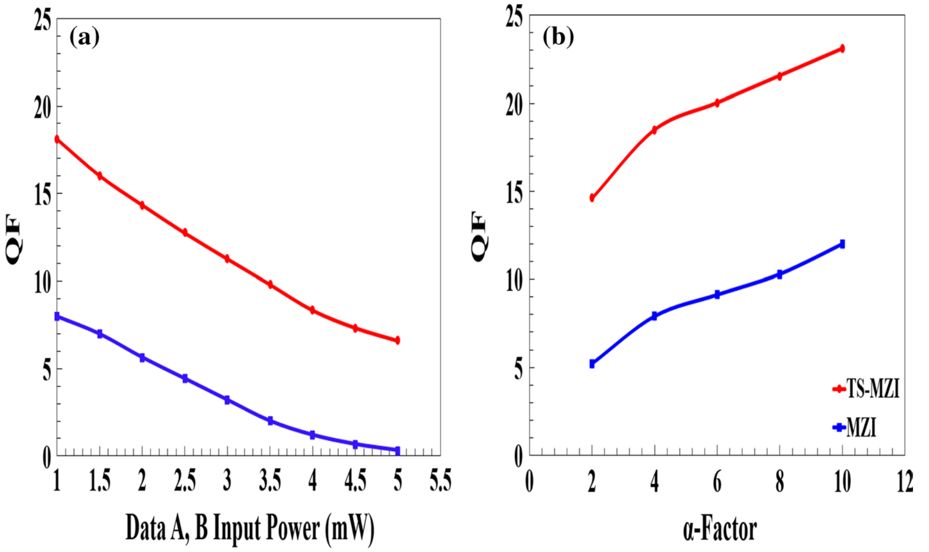

Fig. 8 QF versus **a** data A, B input peak power, **b** QDSOAs traditional linewidth enhancement factor (α-factor), for XOR operation using QDSOA-based TS-MZI and standard MZI at 1 Tb/s

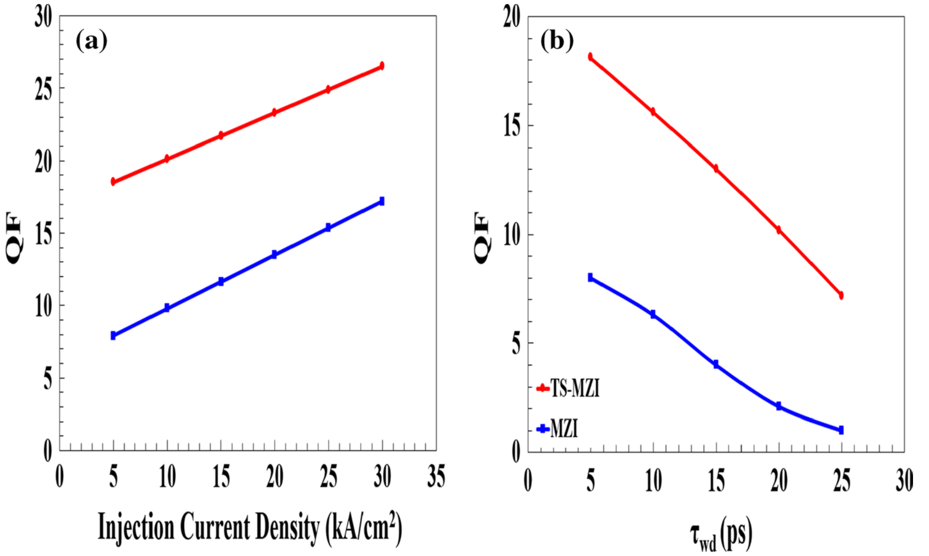

Fig. 9 QF versus QDSOAs **a** injection current density, **b** transition rate from WL to QDs ground state, for XOR operation QDSOA-based TS-MZI and standard MZI at 1 Tb/s

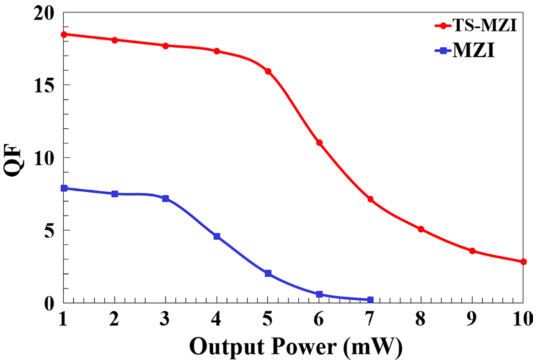

Fig. 10 QF versus QDSOA-based TS-MZI and standard MZI output power for XOR operation at 1 Tb/s

have been obtained for both TS-MZI and conventional MZI schemes. From the observation of these curves, we can make the following important remarks:

(1) The exploitation of the TS is beneficial for the performance of the AO gates since for all varying parameters the QF is acceptable. In contrast, without the TS, this either cannot happen unless the examined parameters are carefully chosen, or it can happen only marginally without selection freedom.

(2) Using the TS allows obtaining a higher QF when the requirements for the key QDSOAs parameters are relaxed, unlike when not resorting to the specific architecture. Specifically, we can employ QDSOAs that exhibit smaller linewidth enhancement factor, are

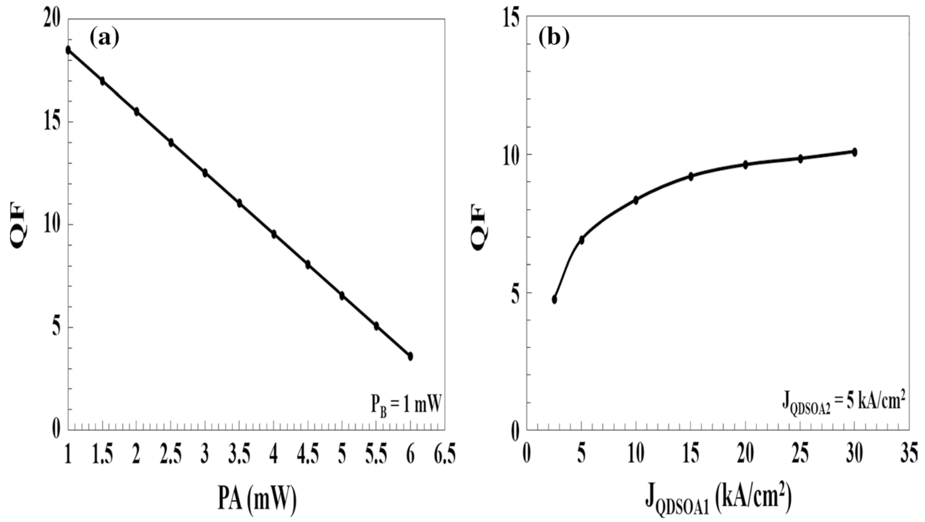

Fig. 11 QF versus QDSOA1 **a** launched power of data signal A (PA), **b** injection current density (J) for XOR operation at 1 Tb/s

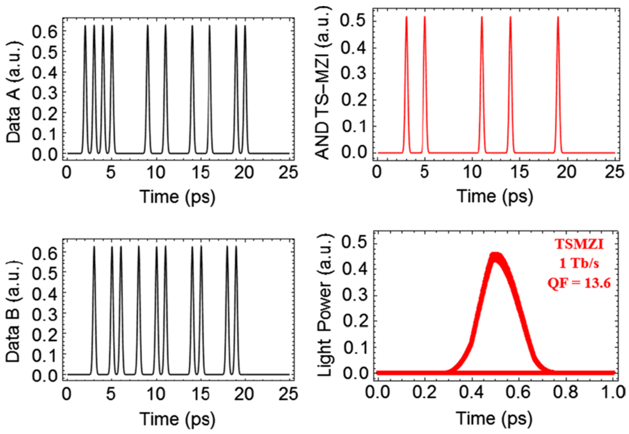

Fig. 12 Simulation results for AND operation with QDSOA-based TS-MZI at 1 Tb/s

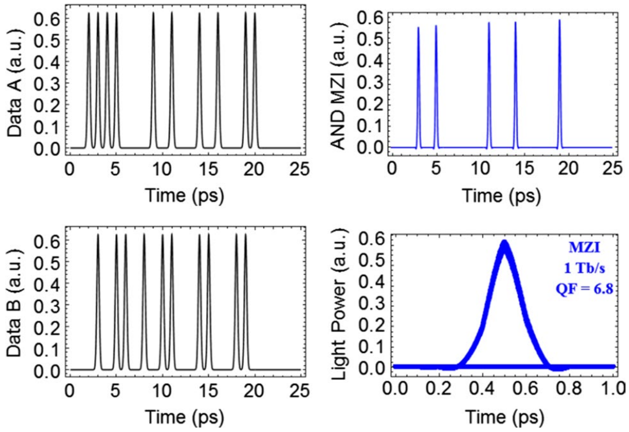

Fig. 13 Simulation results for AND operation with QDSOA-based MZI at 1 Tb/s

biased with less current, and undergo slower transitions between their QDs states. These characteristics are attractive from a practical perspective as they enable to design the AO gates in a more flexible, controllable, and affordable manner.

(3) Owing to the TS inherent capability to efficiently resolve for pattern dependencies, input data pulses can be more intense and still be switched without being degraded by associated pattern effects induced due to QDSOAs heavier saturation. This fact can make the difference in cascaded AO gates applications, where the power level of the signal switched from each gate is expected to be such that it can drive the next identical gate [47].

Figure 10 shows the QF variation versus the power obtained at the output of the QDSOA-based TS-MZI and standard MZI. From this figure, it can be seen that although the QF of both schemes declines if higher output power is pursued, the performance of the TS-MZI is superior to its conventional counterpart for the same output power, while the QF remains acceptable for a range of this quantity being more than 3 dB wider.

Figure 11 shows the QF obtained for the XOR operation when varying (a) the power of data signal A (PA) launched into QDSOA1 and (b) the current density of QDSOA1 (J_{QDSOA1}), when the corresponding parameters of QDSOA2 are kept fixed to their default values given in Table 1. From this figure, it can be seen that in order to obtain at least the minimum acceptable QF = 6 the power mismatch between data signals A and B must not exceed 7 dB, while the current densities of these active devices can differ by as much as 0.8 kA/cm^2, which is equivalent to an asymmetric bias current of 4 MA. In practice, the impact of any such discrepancies can be compensated for by employing after QDSOA3 and QDSOA4 active phase shifters to provide an extra phase

Fig. 14 QF versus **a** data input peak power, **b** QDSOAs traditional linewidth enhancement factor (α-factor), for AND operation using QDSOA-based TS-MZI and standard MZI at 1 Tb/s

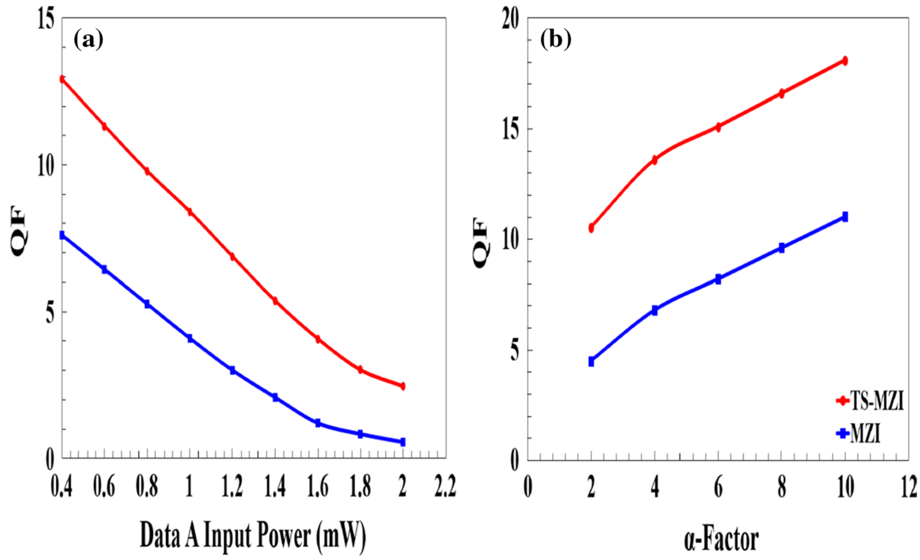

Fig. 15 QF versus QDSOAs **a** injection current density, **b** transition rate from WL to QDs ground state, for AND operation QDSOA-based TS-MZI and standard MZI at 1 Tb/s

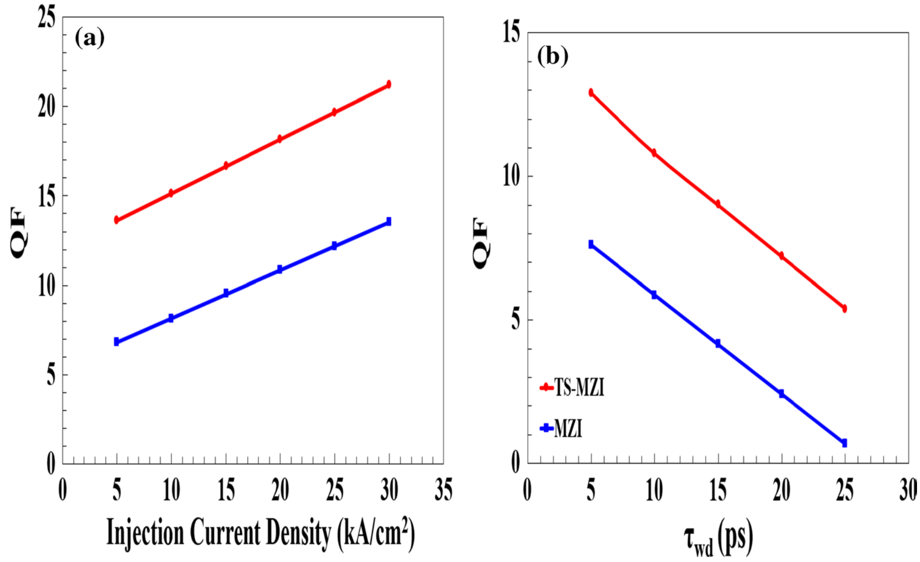

bias between the upper and lower MZI arms [48] and thus adjust the total phase difference required for switching.

4.2 AND

Figures 12 and 13 show the simulation results for the logic pulse profiles and corresponding PEDs for the AO AND operation using the QDSOA-TS-MZI and the QDSOA-MZI at 1 Tb/s. The obtained QFs are 13.6 and 6.8, respectively, where the same note as for the XOR gate holds regarding the very high value of the first QF. Thanks to the TS-MZI, the Boolean AND operation can be executed all-optically with pattern-free logical correctness and with a higher QF than

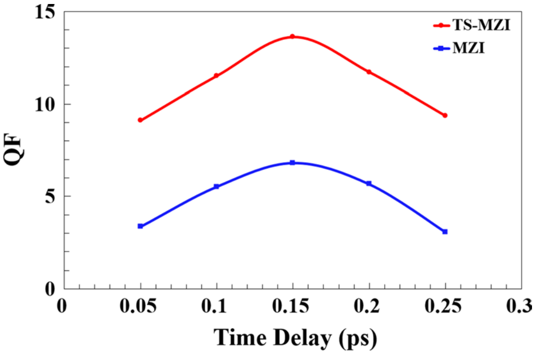

Fig. 16 QF versus temporal offset of delayed signal A, for AND operation using QDSOA-based TS-MZI and standard MZI at 1 Tb/s

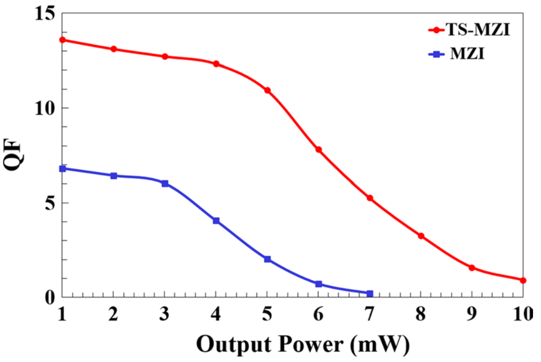

Fig. 17 QF versus QDSOA-based TS-MZI and standard MZI output power for AND operation at 1 Tb/s

with the standard MZI. The XC is 93%, which indicates that the switched data pulse envelope deviates by only 7% from that inserted in the configuration. The XC is 87% when using the conventional MZI.

Figures 14 and 15 illustrate the QF against the parameters which have been defined as critical throughout this treatment (see the corresponding point in Sect. 4.1), with the addition of the temporal offset of the delayed version of data signal A (Fig. 16). It can be seen that for the set of parameters examined in the previous section the curves have a form and follow a trend, similar to that visualized therein, while the drawn conclusions (1)–(3) also hold qualitatively. It is also seen that the QF remains permissible across the whole scanned span for the TS-MZI, while this extent is narrower for the conventional MZI. Moreover, Fig. 16 exhibits a bell-like shape, with the QF acquiring a local maximum for a time delay of 0.15 ps, on either side of which it declines. The physical explanation for this fact is that [19] for shorter values of time delay, the phase switching window created by the differential TS-based scheme becomes less open for the switching bits to lie within it, which affects negatively the QF. When, on the other hand, the time delay is increased then the input and delayed pulses lose their relative synchronization, which impairs the magnitude of the phase switching window and accordingly the QF. There exists, thus a time delay that compromises these two extremes and optimizes the QF.

Figure 17 shows the QF variation versus the power obtained at the output of the QDSOA-based TS-MZI and standard MZI. From this figure, it can be seen that the same qualitative observations as those made for Fig. 10 hold.

5 Conclusion

The performance of all-optical XOR and AND Boolean functions using quantum-dot semiconductor optical amplifiers (QDSOAs) incorporated either in the turbo-switched (TS) or the conventional Mach–Zehnder interferometers (MZIs) was theoretically studied at 1 Tb/s. The dependence of the quality factor on the data input and QDSOAs critical parameters was investigated and assessed. The obtained results indicate that the considered Boolean functions can be realized at the target data rate with higher performance and under better-operating conditions using QDSOAs in the TS-MZI rather than in the standard MZI scheme. Therefore, the QDSOA-based TS-MZI can allow the AO XOR and AND gates to keep pace with the evolving trend in ultrafast line rates in a feasible and competent manner.

Acknowledgements This work was funded by the Chinese Academy of Sciences President’s International Fellowship Initiative (Grant No. 2019FYT0002) and Talented Young Scientist Program supported by the China Science and Technology Exchange Center of Ministry of Science and Technology of China.

References

1. Berrettini, G., Malacarne, A., Prati, G.: OTDM-based optical communications networks at 160 Gbit/s and beyond. Opt. Fiber Technol. **13**, 1–12 (2007)
2. Mulvad, H.C.H., Galili, M., Oxenløwe, L.K., Hu, H., Clausen, A.T., Lensen, J.B., Peucheret, C., Jeppesen, P.: Demonstration of 5.1 Tbit/s data capacity on a single-wavelength channel. Opt. Express **18**, 1438–1443 (2010)
3. Willner, A.E., Khaleghi, S., Chitgarha, M.R., Yilmaz, O.F.: All-optical signal processing. J. Lightwave Technol. **32**, 660–680 (2014)
4. Singh, S., Kaur, R., Kaler, R.S.: Photonic processing for all-optical logic gates based on semiconductor optical amplifiers. Opt. Eng. **53**, 116102 (2014)
5. Zhang, X., Li, W., Hu, H., Dutta, N.K.: High-speed all-optical encryption and decryption based on two-photon absorption in semiconductor optical amplifiers. Opt. Commun. Netw. **7**, 276–285 (2015)
6. Thapa, S., Zhang, X., Dutta, N.K.: Effects of two-photon absorption on pseudo-random bit sequence operating at high speed. J. Mod. Opt. **66**, 100–108 (2019)
7. Zoiros, K.E.: Special issue on applications of semiconductor optical amplifiers. Appl. Sci. **8**, 1185 (2018)
8. Mørk, J., Nielsen, M.L., Berg, T.W.: The dynamics of semiconductor optical amplifiers: modeling and applications. Opt. Photon. News **14**, 42–48 (2003)
9. Manning, R.J., Yang, X., Webb, R.P., Giller, R., Gunning, F.C.G., Ellis, A.D.: The ‘turbo-switch’—a novel technique to increase the high-speed response of SOAs for wavelength conversion. In: Proceedings of Optical Fiber Communication Conference, 2006. Art. No. 1636676 (2006)
10. Manning, R.J., Giller, R., Yang, X., Webb, R.P., Cotter, D.: Faster switching with semiconductor optical amplifiers. In: Proceedings of Photonics in Switching 2007, pp. 145–146. Art. No. 4300786 (2007)
11. Nielsen, M., Mørk, J.: Bandwidth enhancement of SOA-based switches using optical filtering: theory and experimental verification. Opt. Express **14**, 1260–1265 (2006)
12. Weng, Q., Yang, X., Hu, W.: Theoretical analysis of high-speed all-optical turbo-switches. IEEE J. Sel. Top. Quantum Electron. **18**, 662–669 (2012)
13. Zhou, P., Yang, X., Hu, X., Hu, W.: Bandwidth analysis of all-optical turbo-switch. Opt. Commun. **334**, 105–109 (2015)

14. Reid, D.A., Clarke, A.M., Yang, X., Maher, R., Webb, R.P., Manning, R.J., Barry, L.P.: Characterization of a turbo-switch SOA wavelength converter using spectrographic pulse measurement. IEEE J. Sel. Top. Quantum Electron. **14**, 841–848 (2008)
15. Yang, X., Mishra, A.K., Manning, R.J., Giller, R.: All-optical 40 Gbit/s NRZ to RZ format conversion by nonlinear polarisation rotation in SOAs. Electron. Lett. **43**, 469–470 (2007)
16. Yang, X., Weng, Q., Hu, W.: High-speed, all-optical XOR gates using semiconductor optical amplifiers in ultrafast nonlinear interferometers. Front. Optoelectron. China **3**, 245–252 (2010)
17. Gutiérrez-Castrejón, R.: Turbo-switched Mach-Zehnder interferometer as all-optical signal processing element at 160 Gb/s. Opt. Commun. **282**, 4345–4352 (2009)
18. Rendón-Salgado, I., Gutiérrez-Castrejón, R.: 160 Gb/s all-optical AND gate using bulk SOA turbo-switched Mach–Zehnder interferometer. Opt. Commun. **399**, 77–86 (2017)
19. Rendón-Salgado, I., Ramírez-Cruz, E., Gutiérrez-Castrejón, R.: 640 Gb/s all-optical AND gate and wavelength converter using bulk SOA turbo-switched Mach–Zehnder interferometer with improved differential scheme. Opt. Laser Technol. **109**, 671–681 (2019)
20. Schreieck, R.P., Kwakernaak, M.H., Jäckel, H., Melchior, H.: All-optical switching at multi-100-Gb/s data rates with Mach–Zehnder interferometer switches. IEEE J. Quantum Electron. **38**, 1053–1061 (2002)
21. Sugawara, M., Akiyama, T., Hatori, N., Nakata, Y., Ebe, H., Ishikawa, H.: Quantum-dot semiconductor optical amplifiers for high-bit-rate signal processing up to 160 Gbps-1 and a new scheme of 3R regenerators. Meas. Sci. Technol. **13**, 1683–1691 (2002)
22. Berg, T.W., Mørk, J.: Saturation and noise properties of quantum-dot optical amplifiers. IEEE J. Quantum Electron. **40**, 1527–1539 (2004)
23. Akiyama, T., Ekawa, M., Sugawara, M., Kawaguchi, K., Sudo, H., Kuramata, A., Ebe, H., Arakawa, Y.: An ultrawide-band semiconductor optical amplifier having an extremely high penalty-free output power of 23 dBm achieved with quantum-dots. IEEE Photon. Technol. Lett. **17**, 1614–1616 (2005)
24. Yasuoka, N., Kawaguchi, K., Ebe, H., Akiyama, T., Ekawa, M., Morito, K., Sugawara, M., Arakawa, Y.: Quantum-dot semiconductor optical amplifiers with polarization-independent gains in 1.5-μm wavelength bands. IEEE Photon. Technol. Lett. **20**, 1908–1910 (2008)
25. Zilkie, A.J., Meier, J., Mojahedi, M., Poole, P.J., Barrios, P., Poitras, D., Rotter, T.J., Yang, C., Stintz, A., Malloy, K.J., Smith, P.W.E., Aitchison, J.S.: Carrier dynamics of quantum-dot, quantum-dash and quantum-well semiconductor optical amplifiers operating at 1.55 μm. IEEE J. Quantum Electron. **43**, 982–991 (2007)
26. Ben-Ezra, Y., Lembrikov, B.I., Haridim, M.: Ultrafast all-optical processor based on quantum-dot semiconductor optical amplifiers. IEEE J. Quantum Electron. **45**, 34–41 (2009)
27. Ma, S., Chen, Z., Sun, H., Dutta, N.K.: High-speed all-optical logic gates based on quantum-dot semiconductor optical amplifiers. Opt. Express **18**, 6417–6422 (2010)
28. Rostami, A., Nejad, H., Qartavol, R., Saghai, H.: Tb/s optical logic gates based on quantum-dot semiconductor optical amplifiers. IEEE J. Quantum Electron. **46**, 354–360 (2010)
29. Dimitriadou, E., Zoiros, K.E.: All-optical XOR gate using single quantum-dot SOA and optical filter. J. Lightwave Technol. **31**, 3813–3821 (2013)
30. Dimitriadou, E., Zoiros, K.E.: On the feasibility of 320 Gb/s all-optical AND gate using quantum-dot semiconductor optical amplifier-based Mach–Zehnder interferometer. PIERS B **50**, 113–140 (2013)
31. Kotb, A., Zoiros, K.E.: 1 Tb/s high-quality factor NAND gate using quantum-dot semiconductor optical amplifiers in Mach–Zehnder interferometer. J. Comput. Electron. **13**, 555–561 (2014)
32. Zhang, X., Dutta, N.K.: Effects of two-photon absorption on all-optical logic operation based on quantum-dot semiconductor optical amplifiers. J. Mod. Opt. **65**, 166–173 (2018)
33. Hu, H., Zhang, X., Zhao, S.: High-speed all-optical logic gate using QD-SOA and its application. Cogent Phys. **4**, 1388156 (2018)
34. Li, W., Hu, H., Zhang, X., Dutta, N.K.: High speed all optical logic gates using binary phase shift keyed signal based on QD-SOA. Inter. J. High Speed Electron. Syst. **24**, 1550005 (2015)
35. Pato, S.V., Meleiro, R., Fonseca, D., André, P., Monteiro, P., Silva, H.: All-optical burst-mode power equalizer based on cascaded SOAs for 10-Gb/s EPONs. IEEE Photon. Technol. Lett. **20**, 2078–2080 (2008)
36. Ueno, Y., Nakamura, S., Tajima, K.: Nonlinear phase shifts induced by semiconductor optical amplifiers with control pulses at repetition frequencies in the 40–160-GHz range for use in ultrahigh-speed all-optical signal processing. J. Opt. Soc. Am. B **19**, 2573–2589 (2002)
37. Dutta, N.K., Wang, Q.: Semiconductor optical amplifiers, 2nd edn. World Scientific Publishing Company, Singapore (2013)
38. Cassioli, D., Scotti, S., Mecozzi, A.: A time-domain computer simulator of the nonlinear response of semiconductor optical amplifiers. IEEE J. Quantum Electron. **36**, 1072–1080 (2000)
39. Schares, L., Schubert, C., Schmidt, C., Weber, H.G., Occhi, L., Guekos, L.: Phase dynamics of semiconductor optical amplifiers at 10 to 40 GHz. IEEE J. Quantum Electron. **39**, 1394–1408 (2003)
40. Komatsu, K., Hosoya, G., Yashima, H.: All-optical logic NOR gate using a single quantum-dot SOA-assisted an optical filter. Opt. Quantum Electron. **50**, 131 (2018)
41. Xu, J., Zhang, X., Mørk, J.: Investigation of patterning effects in ultrafast SOA-based optical switches. IEEE J. Quantum Electron. **46**, 87–94 (2010)
42. Agrawal, G.P., Olsson, N.A.: Self-phase modulation and spectral broadening of optical pulses in semiconductor laser amplifiers. IEEE J. Quantum Electron. **25**, 2297–2306 (1989)
43. Yariv, A.: Universal relations for coupling of optical power between microresonators and dielectric waveguides. Electron. Lett. **36**, 321–322 (2000)
44. Rizou, Z.V., Zoiros, K.E., Hatziefremidis, A.: Comparison of basic notch filters for semiconductor optical amplifier pattern effect mitigation. Appl. Sci. **7**, 783 (2017)
45. Matera, F., Settembre, M.: Role of Q-factor and of time jitter in the performance evaluation of optically amplified transmission systems. IEEE J. Sel. Top. Quantum Electron. **6**, 308–316 (2000)
46. Zoiros, K.E., Papadopoulos, G., Houbavlis, T., Kanellos, G.T.: Theoretical analysis and performance investigation of ultrafast all-optical Boolean XOR gate with semiconductor optical amplifier-assisted Sagnac interferometer. Opt. Commun. **258**, 114–134 (2006)
47. Dimitriadou, E., Zoiros, K.E.: On the feasibility of ultrafast all-optical NAND gate using single quantum-dot semiconductor optical amplifier-based Mach–Zehnder interferometer. Opt. Laser Technol. **44**, 1971–1981 (2012)
48. Leuthold, J., Besse, P.A., Eckner, J., Gamper, E., Dulk, M., Melchior, H.: All-optical space switches with gain and principally ideal extinction ratios. IEEE J. Quantum Electron. **34**, 622–633 (1998)